The Astrophysical Journal, 854:128 (15pp), 2018 February 20 https://doi.org/10.3847/1538-4357/aaa890

The Sloan Digital Sky Survey Reverberation Mapping Project: The C IV Blueshift, Its Variability, and Its Dependence Upon Quasar Properties

Mouyuan Sun[1,2], Yongquan Xue[1,2], Gordon T. Richards[3], Jonathan R. Trump[4], Yue Shen[5,6,10], W. N. Brandt[7,8,9], and D. P. Schneider[7,8]

[1] CAS Key Laboratory for Research in Galaxies and Cosmology, Department of Astronomy, University of Science and Technology of China, Hefei 230026, People's Republic of China; ericsun@ustc.edu.cn
[2] School of Astronomy and Space Science, University of Science and Technology of China, Hefei 230026, People's Republic of China; xuey@ustc.edu.cn
[3] Department of Physics, Drexel University, 3141 Chestnut Street, Philadelphia, PA 19104, USA
[4] Department of Physics, University of Connecticut, Storrs, CT 06269, USA
[5] Department of Astronomy, University of Illinois at Urbana-Champaign, Urbana, IL 61801, USA
[6] National Center for Supercomputing Applications, University of Illinois at Urbana-Champaign, Urbana, IL 61801, USA
[7] Department of Astronomy and Astrophysics, 525 Davey Lab, The Pennsylvania State University, University Park, PA 16802, USA
[8] Institute for Gravitation and the Cosmos, 525 Davey Lab, The Pennsylvania State University, University Park, PA 16802, USA
[9] Department of Physics, 104 Davey Lab, The Pennsylvania State University, University Park, PA 16802, USA
Received 2017 November 11; revised 2018 January 11; accepted 2018 January 15; published 2018 February 20

Abstract

We use the multi-epoch spectra of 362 quasars from the Sloan Digital Sky Survey Reverberation Mapping project to investigate the dependence of the blueshift of C IV relative to Mg II on quasar properties. We confirm that high-blueshift sources tend to have low C IV equivalent widths (EWs), and that the low-EW sources span a range of blueshift. Other high-ionization lines, such as He II, also show similar blueshift properties. The ratio of the line width (measured as both the full width at half maximum and the velocity dispersion) of C IV to that of Mg II increases with blueshift. Quasar variability enhances the connection between the C IV blueshift and quasar properties (e.g., EW). The variability of the Mg II line center (i.e., the wavelength that bisects the cumulative line flux) increases with blueshift. In contrast, the C IV line center shows weaker variability at the extreme blueshifts. Quasars with the high-blueshift C IV lines tend to have less variable continuum emission, when controlling for EW, luminosity, and redshift. Our results support the scenario that high-blueshift sources tend to have large Eddington ratios.

Key words: black hole physics – galaxies: active – quasars: emission lines – quasars: general – surveys

Supporting material: animation

1. Introduction

Broad emission lines (hereafter BELs) from the "broad line region" (BLR) are unambiguous features in quasar spectra. These BELs can be divided into two main categories based upon their ionization potential: high-ionization BELs (e.g., C IV, He II) with ionization energy $E_{\rm ion} \gtrsim 50$ eV, and low-ionization BELs (e.g., Hα, Hβ, Mg II) with ionization energy $E_{\rm ion} \lesssim 50$ eV. Compared with low-ionization BELs, high-ionization BELs are believed to be produced closer to the central supermassive black holes (SMBHs). Interestingly, high-ionization BELs, such as C IV, are often significantly shifted blueward with respect to their low-ionization counterparts (e.g., Gaskell 1982; Wilkes 1986; Corbin 1990; Sulentic et al. 2000a, 2007; Richards et al. 2002, 2011; Baskin & Laor 2005; Shen et al. 2008; Wang et al. 2011; Denney 2012; Shen & Liu 2012; Coatman et al. 2016, 2017). The blueshift velocity can be as large as $\sim$8000 km s^{-1} (e.g., Luo et al. 2015). This result raises several important questions, including the origin of the blueshift, its effect on the estimation of the mass of the central SMBHs ($M_{\rm BH}$), and its role in quasar unification.

The blueshift is often attributed to accretion-disk winds (e.g., Gaskell 1982; Murray & Chiang 1997; Proga et al. 2000; Leighly 2004; Leighly et al. 2007; Richards et al. 2011; Denney 2012; Chajet & Hall 2013). Such winds can disturb the velocity field of the BLR material and therefore can affect the line profiles. An alternative possibility is that the blueshift is due to the scattering between the inflowing gases and the BEL photons (Gaskell 2009). There are also speculations that the blueshift arises due to radiative transfer effects (Richards et al. 2002).

Different physical drivers can be assessed using correlations of blueshift with quasar properties. For instance, it is likely that high-blueshift quasars favor distinct regions of quasar parameter space or the quasar Eigenvector 1 sequence (Boroson & Green 1992; Sulentic et al. 2000b, 2017; Dong et al. 2009; Runnoe et al. 2014; Shen & Ho 2014), e.g., high Eddington ratios $\lambda_{\rm Edd}$ (Baskin & Laor 2005; Coatman et al. 2016), soft (i.e., with weak X-ray emission) spectral energy distributions (SEDs; see, e.g., Leighly 2004; Richards et al. 2011; Luo et al. 2015), low inclination angles (Denney 2012), and/or low variability.

In addition to the origin of the blueshift and its correlation with quasar properties, it is also important to consider the effects of the blueshift on $M_{\rm BH}$ estimation. As noted by Richards et al. (2011), the widely adopted single-epoch black-hole mass estimators (e.g., Vestergaard & Peterson 2006; Vestergaard & Osmer 2009; Shen et al. 2011; for a recent review, see Shen 2013a) are derived using a low-blueshift reverberation-mapped quasar sample. There are two reasons why such estimators might not be valid for high-blueshift quasars. First, as mentioned before, the observed line profiles are likely due to a mixture of virial (i.e., dominated by the gravitational potential of the central SMBHs) and non-virial

[10] Alfred P. Sloan Research Fellow.

motions. Second, there are indications that the empirical BLR radius-quasar optical luminosity relation for Hβ depends on quasar SEDs (Kilerci Eser et al. 2015) and/or Eddington ratios (Du et al. 2016). If the high-blueshift quasars indeed occupy a distinct region of quasar parameter space, the current radius–luminosity relation could be invalid for those quasars.

The blueshift was not the first BEL feature showing significant changes across the quasar distribution. Rather, that was the well-known Baldwin Effect (Baldwin 1977), which represents an anti-correlation between the C IV EW and luminosity (e.g., Dietrich et al. 2002; Wu et al. 2009). Weak BEL quasars also tend to show large C IV blueshifts (e.g., Marziani et al. 1996, 2016; Richards et al. 2011; Plotkin et al. 2015). Hence, there could be possible connections between the C IV blueshift and EW. It is now well-established that *both* the EW and blueshift are needed to minimally characterize the range of properties exhibited by C IV (Sulentic et al. 2007; Richards et al. 2011; Marziani et al. 2016).

In this work, we explore the high-ionization BEL blueshift phenomenon taking advantage of the first 32 epochs of spectra from the Sloan Digital Sky Survey Reverberation Mapping project (SDSS-RM; for a technical overview, see Shen et al. 2015). Compared with previous works, the SDSS-RM project provides a high S/N composite spectrum for each of the 849 quasars, allowing us to accurately measure the blueshift for both strong and weak emission lines. By analyzing the spectra epoch by epoch, we can also measure the variability properties of the blueshift. Finally, understanding the blueshift properties of the SDSS-RM sample is also crucial for the project since one of its main goals is to provide unbiased $M_{\rm BH}$ estimators for a wide variety of quasars.

This paper is formatted as follows. In Section 2, we discuss our spectral fitting procedures, and our measurements of quasar properties. In Section 3, we show our analysis of the high S/N composite spectra. In Section 4, we present measurements of the variability of the blueshift. In Section 5, we discuss the implication of our results. A summary of our work appears in Section 6. We adopt a flat ΛCDM cosmology with $h_0 = 0.7$ and $\Omega_{\rm M} = 0.3$. Throughout this work, the wavelengths of quasar features always refer to the rest-frame, unless otherwise specified.

2. Spectral Measurement

The SDSS-RM project is an ancillary program within the SDSS-III (Eisenstein et al. 2011) BOSS survey (Dawson et al. 2013) using a dedicated 2.5 m telescope at Apache Point Observatory (Gunn et al. 2006). The spectrograph has a wavelength range of 3650–10400 Å with a spectral resolution of $R \sim 2000$ (Smee et al. 2013). Each of the 32 epochs has a typical exposure time of 2 hr. The spectra were pipeline-processed (Bolton et al. 2012) and were flux calibrated via a custom scheme (Shen et al. 2015). The SDSS-RM sample consists of 849 BEL quasars. We only select $1.48 < z < 2.6$ sources for which Mg II and C IV were both covered in the BOSS spectra. We focus on 29 (three of the 32 epochs are discarded due to low S/Ns) epochs of the SDSS-RM (Shen et al. 2015) spectra and the resulting high S/N composite spectra. As mentioned in Shen et al. (2015) and Sun et al. (2015), there are spectra with flux anomalies.[11] An epoch was identified as an outlier if its flux is more than 1 magnitude away from the median of all epochs (Sun et al. 2015). These outliers are rejected. Below we explain our spectral fitting approach.

2.1. Spectral Fitting

2.1.1. Continuum Fitting

Our spectral-fitting approach is similar to that of Trump et al. (2009) and Shen et al. (2011). For each spectrum, we first fit a double power-law continuum (i.e., $f_\lambda = A_1\lambda_1^{\beta}$ if $\lambda < 2000$ Å; $f_\lambda = A_2\lambda^{\beta_2}$ if $\lambda > 2000$ Å) plus a broadened iron template (Vestergaard & Wilkes 2001) to the following relatively emission-line-free wavelength ranges, 1445 Å $< \lambda <$ 1465 Å, 1700 Å $< \lambda <$ 1705 Å, 2200 Å $< \lambda <$ 2700 Å, and 2900 Å $< \lambda <$ 3088 Å. During the continuum and the subsequent emission-line fitting, we rejected data points that were 3σ below the 30-pixel boxcar-smoothed spectrum. The purpose of this procedure is to reduce the effects of narrow absorption lines. We performed an iterative χ^2 minimization[12] to optimize the fits. The continuum and iron best fit is then subtracted from the spectrum. We then fit the resulting line spectrum with several Gaussian functions. In the following sections, we present our modeling procedures for Mg II and C IV (and He II λ1640).

2.1.2. Line Fitting

Mg II: We fit the continuum- and iron-subtracted flux in the wavelength range of 2700 Å $< \lambda <$ 2900 Å with three Gaussian functions, each with an unconstrained full-width at half maximum (FWHM), i.e., we do not consider narrow Mg II subtraction. We calculate the Mg II line-profile properties from the overall line profile, which is the summation of the multiple best-fit Gaussian functions. Any Gaussian function with the ratio of its flux to the total line flux <0.05 is ignored.

C IV: We adopted different line-modeling procedures for the composite and single-epoch spectra.

For the composite data, the pseudo-continuum subtracted spectrum from 1500 Å $< \lambda <$ 1700 Å was modeled with six Gaussian functions: two Gaussians for C IV, two Gaussians for He II λ1640, and the remaining two Gaussians for O III] λ1663. Therefore, the 1600 Å feature of the composite data is modeled by the superposition of the red tail of C IV and a broad He II. This approach is similar to some previous studies (e.g., Fine et al. 2010; Marziani et al. 2010). Similar to that of Mg II, we do not set limits on the FWHMs of the Gaussian functions.

For the single-epoch spectra, we only considered the following wavelength range: 1500 Å $< \lambda <$ 1600 Å. The resulting pseudo-continuum subtracted spectrum was fitted with two Gaussian functions. We do not model either He II or O III] since the main purpose of the single-epoch spectral fitting is to constrain the variability of line properties. The measurement errors of He II or O III] are relatively large since the two lines are weak. Therefore, it is nontrivial to reliably constrain the intrinsic variability of their line properties.

Similar to Mg II, any Gaussian function with the ratio of its flux to the total flux <0.05 is removed from consideration when calculating the line-profile properties.

[11] As noted by Shen et al. (2015), such spectra might be obtained due to the dropping of the fiber during spectroscopic exposures.

[12] We use *kmpfit*, a Python version of the least squares fit routine, to perform our fitting. This routine is available as a part of the Kapteyn package, which can be downloaded from http://www.astro.rug.nl/software/kapteyn/.

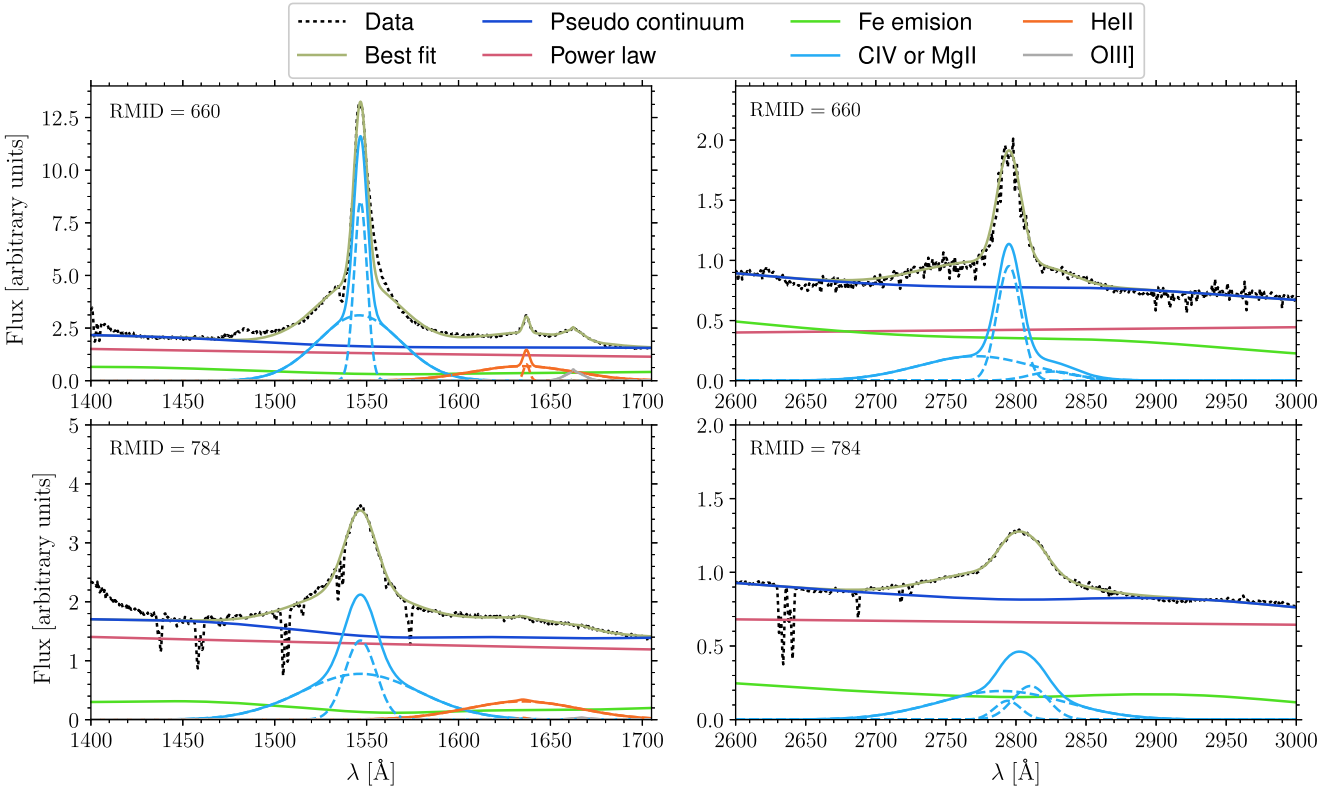

Figure 1. Examples of multi-component fits to the composite spectra. The upper and lower panels are for RMID = 660 and 784, respectively. The left and right panels are for C IV (with He II and O III]) and Mg II, respectively.

In Figure 1, we present examples of our fits to the high S/N composite spectra of RMID[13] = 660 and RMID = 784.

2.1.3. Uncertainty Estimation

We adopted a Monte Carlo approach to estimate the uncertainties of the spectral-fitting parameters. A total of 100 (50 for single-epoch spectra) mock spectra were synthesized, where the flux in each wavelength pixel was generated by adding the flux density noise to the best-fit models. We then fit the mock spectra following the same fitting recipe. The uncertainties are estimated from the statistical dispersion of the best-fit models of the mock spectra. The statistical dispersion was estimated by 0.74IQR(x), where IQR(x) is the interquartile range (IQR) of the variable x. The constant 0.74 normalizes the IQR to be equivalent to the standard deviation of a Gaussian distribution. Unlike the standard deviation, the IQR is robust against outliers or tails in the distribution.

Following Shen et al. (2013b), we justified our uncertainty estimation by exploring the distributions of quasar properties between close (i.e., rest-frame time interval <2 days) pairs. We then compared these distributions with the expected ones from the measurement errors. Our Monte Carlo approach underestimated the true uncertainties, so we enlarged the uncertainties by a constant factor until the expected distributions from the measurement errors matched the observed close-pair distributions. The constant factor varies from ∼1.2 to ∼1.7, depending on the physical quantities we are interested in. In the following analyses, we will scale our uncertainties up by the constant factor.

2.2. Emission-line Properties

We calculated the following parameters of the emission-line properties. All line measurements are from the total line profile, which is the sum of the multiple Gaussians (excluding Gaussian components that contribute less than 5% of the total flux).

1. The shift velocity, $V_{\rm shift}$ ($V_{\rm shift,se}$ for the single-epoch data), is defined as $c \times (\lambda_{\rm h} - \lambda_{\rm va})/\lambda_{\rm va}$, where c, $\lambda_{\rm va}$, and $\lambda_{\rm h}$ are the speed of light, the central wavelength of the emission line in vacuum, and the line center. The latter is defined as the wavelength that bisects the cumulative total line flux (Coatman et al. 2017). Figure 2 presents an illustration of the definition of $\lambda_{\rm h}$.
2. The offset of C IV for the coadded spectrum is, $V_{\rm off,C\,IV} = V_{\rm shift,C\,IV} - V_{\rm shift,Mg\,II}$.[14] That is, negative values indicate blueshift toward the observer (i.e., "outflows"). We define the single-epoch offset velocity as $V_{\rm off,se} = V_{\rm shift,C\,IV,se} - V_{\rm shift,Mg\,II}$. The observed variations of $V_{\rm off,se}$ are due to the line-shift variability of C IV. The offsets of other lines are defined in a similar way. Our definition of the offset of C IV might be an underestimation of the true value because Mg II lines also show offsets with respect to Hβ (Marziani et al. 2013) or the host galaxy (e.g., Shen et al. 2016) by a median blueshift velocity of 65 km s^{-1} with an intrinsic scatter of ∼200 km s^{-1}.
3. The emission-line velocity width can be measured by FWHM or dispersion (σ) of the profile. Compared with FWHM, σ is more sensitive to the wing of the emission line.

[13] RMID is the index of sources in the SDSS-RM catalog (see Table 1 of Shen et al. 2015).

[14] We adopted this definition because, for the redshift ranges considered here, Mg II is the best practical redshift estimator (Shen et al. 2016).

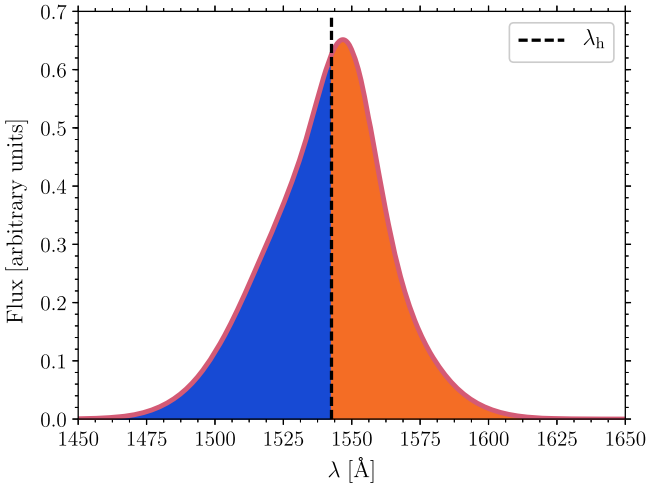

Figure 2. Illustration of the definition of λ_h. That is, the total flux of the wavelengths shortward (i.e., $\lambda < \lambda_h$) equals that of the wavelengths longward (i.e., $\lambda > \lambda_h$).

4. The emission-line shape is defined as $D = \mathrm{FWHM}/\sigma$. For a perfect Gaussian profile, $D = 2.354$. Larger values of D indicate that the profiles are more "boxy."
5. The equivalent width is calculated using $\mathrm{EW} = \int_{\lambda_{va}-200\ \text{Å}}^{\lambda_{va}+200\ \text{Å}} \frac{f_{line}(\lambda)}{f_{cont}(\lambda)} d\lambda$, where $f_{line}(\lambda)$ and $f_{cont}(\lambda)$ are both obtained from our spectral fitting results.

We measured the 1350 Å and the 3000 Å continuum luminosities (hereafter $L1350$ and $L3000$, respectively) from the best-fit double power-law component. We adopted the 1350 Å continuum luminosity multiplied by a monochromatic bolometric correction of 5 (Richards et al. 2006) as an estimator of the bolometric luminosity, $L_{\rm Bol}$.[15]

We adopt the Mg II virial estimator to measure $M_{\rm BH}$ (see Equation (8) of Shen et al. 2011. The Eddington ratio is $\lambda_{\rm Edd} = L_{\rm Bol}/(1.26 \times 10^{38}\, M_{\rm BH}/M_\odot\ \mathrm{erg\ s^{-1}})$.

2.3. Sample Properties

We flagged our fits to the composite spectra by visual inspection. The spectra of quasars for which reliable emission-line parameters could not be estimated are rejected. These spectra contain strong broad absorption lines, or have multiple absorption features around the line centers of Mg II or C IV. Our final sample consists of 362 sources. In Figure 3, we present the distribution of $L_{\rm Bol}$ as a function of redshift for this sample. The quasar luminosity, $M_{\rm BH}$ and $\lambda_{\rm Edd}$ ranges span two orders of magnitude, and therefore it is suitable to explore the dependencies of the C IV blueshift upon quasar properties.

3. The Composite Spectra

We are now in a position to explore $V_{\rm off,C\ IV}$ as a function of emission line properties.

3.1. The Blueshift and EW

Figure 4 shows the distribution of our sample in the C IV EW-offset velocity parameter space. The distribution of

[15] Our results do not critically depend on $L_{\rm Bol}$. Therefore, our conclusions do not change if we instead adopt luminosity-dependent bolometric correction factors (e.g., Lusso et al. 2012; Krawczyk et al. 2013).

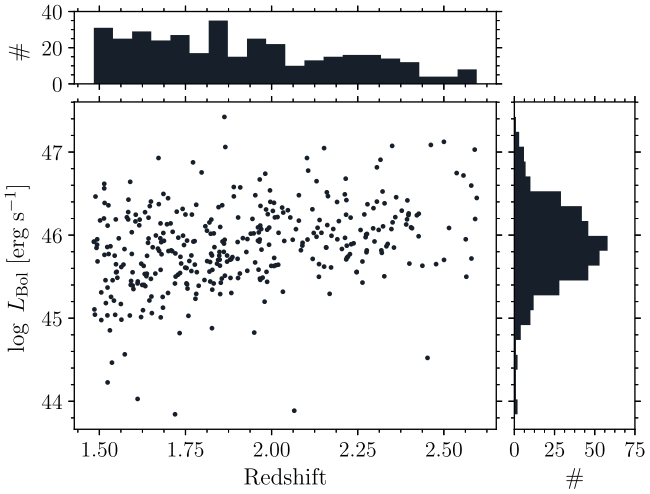

Figure 3. Distribution of our sample in the $L_{\rm Bol}$–redshift plane. Our sample consists of 362 sources with $1.48 < z < 2.6$. The quasar luminosity range spans two orders of magnitude.

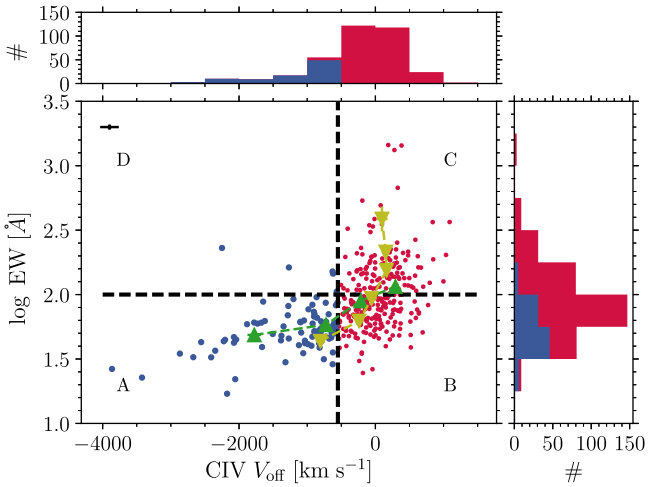

Figure 4. Distribution of our sample in the C IV offset velocity-EW plane. Sources with offset velocity < -550 km s^{-1} are highlighted by blue colors. The green (yellow) triangles represent the mean log EW (C IV $V_{\rm off}$) in each C IV $V_{\rm off}$ (log EW) bin. It is clear that the high-blueshift quasars tend to have small EWs. However, the scatter of the correlation is not negligible. We defined three samples A, B, and C, according to the distribution (black dashed lines; see the text). Similar to the results of Richards et al. (2011), our sources tend to avoid the high-blueshift and high-EW (i.e., "D") space. The black cross indicates the typical uncertainties of the C IV offset velocity and EW.

the C IV offset velocity is not symmetric, with a long tail of blueshifted velocities. For instance, ∼5% of sources have $V_{\rm off,C\ IV} > 550$ km s^{-1}, while ∼24% of sources (highlighted as blue dots) have $V_{\rm off,C\ IV} < -550$ km s^{-1}.

We also binned the sources according to the C IV EW or the offset velocity. Consistent with previous works (e.g., Richards et al. 2011; Luo et al. 2015), the sources with extreme C IV blueshifts tend to have weak C IV. However, weak C IV is an insufficient condition for a quasar to have a strong C IV blueshift. We will further discuss the connection between the C IV blueshift and EW in Section 5. Our sources can be divided into three subsamples that will be used in some of the subsequent analyses:

1. Sample A: the "blueshift" subsample, i.e., sources with offset velocities <-550 km s^{-1} and log EW < 2.0 (we selected this limit because 95% of sources with offset

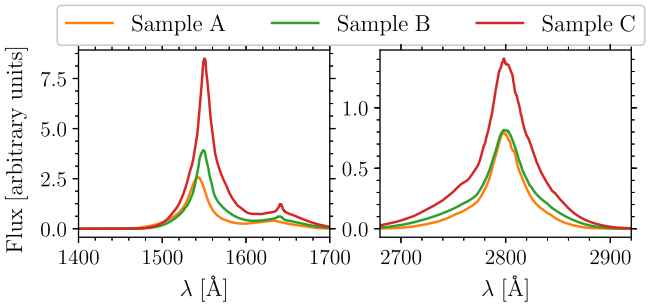

Figure 5. Composite spectra from C IV, He II, and Mg II for the three regions of the C IV offset velocity-EW plane (see Figure 4). The composite spectra are normalized to the best-fitting 2400 Å continuum. We adopted Mg II as the redshift estimator. It is evident that both C IV and He II show blueshift with respect to Mg II. The C IV shape parameter D of Sample A is larger than those of Samples B or C. Therefore, the C IV line profile of Sample A is more boxy than those of Samples B or C.

velocities $<-550\,\mathrm{km\,s^{-1}}$ satisfy this limit). There are 84 sources in this sample.

2. Sample B: sources with offset velocities $>-550\,\mathrm{km\,s^{-1}}$ (i.e., weak or no blueshift) and log EW < 2.0 (i.e., weak C IV). 154 sources belong to this sample.
3. Sample C: sources with offset velocities $>-550\,\mathrm{km\,s^{-1}}$ (i.e., weak or no blueshift) and log EW > 2.0 (i.e., strong C IV). This sample consists of 118 sources.

There are only six sources in the high-blueshift and high-EW space.

We have constructed composite spectra of Mg II, He II, and C IV for samples A, B, and C. The procedures to stack individual spectra into a composite spectrum are as follows. First, we normalize each individual spectrum by its best-fitting 2400 Å continuum flux. Second, for each wavelength, we take the median flux from the best-fitting line profiles of the normalized individual spectra. Third, we shift the wavelength to ensure that $V_{\mathrm{shift,MgII}} = 0$, i.e., we adopt Mg II as the redshift estimator. In Figure 5, we show the three composite spectra of Mg II, He II, and C IV. Both C IV and He II show blueshift with respect to Mg II. The line shapes of C IV and He II also change with the C IV blueshift.

It is interesting that another high ionization line, He II, displays similar properties. Indeed, the He II blueshift (with respect to Mg II) and that of C IV are strongly correlated (Figure 6). We adopted the Bayesian linear regression method in Kelly (2007) to fit the data. The best-fit relation is $y = (0.69 \pm 0.02)x - (583 \pm 20)\,\mathrm{km\,s^{-1}}$ with an intrinsic scatter of $374 \pm 16\,\mathrm{km\,s^{-1}}$, where x and y correspond to the blueshifts of C IV and He II relative to Mg II, respectively.[16] The blueshift velocity of He II is statistically larger than that of C IV.[17] Meanwhile, the slope of the correlation is shallower than the one-to-one relation. Hence, for sources with C IV $V_{\mathrm{off}} < -1000\,\mathrm{km\,s^{-1}}$, the blueshift velocities of C IV are larger than those of He II. The distribution of our sample in the He II EW-offset parameter space is similar to that of C IV (Figure 7). Our correlation is unlikely to be due to possible redshift biases

[16] Unlike Denney et al. (2016) who tried only to include the narrow component, we considered the full He II line (i.e., the summation of broad and narrow profiles). Therefore, it is not straightforward to compare our results with those of Denney et al. (2016).

[17] However, this conclusion depends on the definition of the shift velocity. If we measure the shift velocity via the line peak and do not exclude the components with the ratio of their flux to the total flux <0.05, the blueshift velocity of He II is statistically similar to that of C IV (Shen et al. 2016).

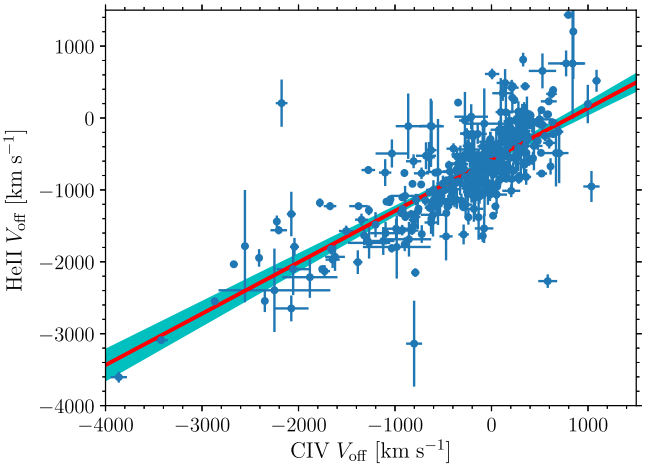

Figure 6. He II offset as a function of the C IV offset (both are relative to Mg II). The red solid line and the shadowed region represent the best-fit relation and its 1σ confidence band. The best-fit relation is $y = (0.69 \pm 0.02)x - (583 \pm 20)$ km s^{-1}, where x and y correspond to the blueshifts of C IV and He II relative to Mg II, respectively. The intrinsic scatter is 374 ± 16 km s^{-1}.

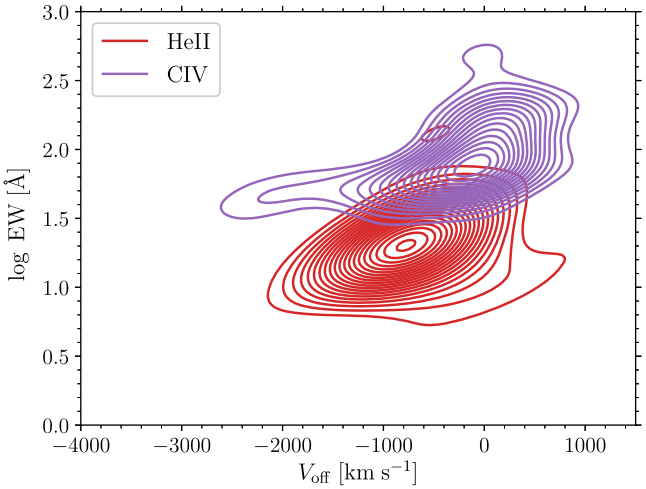

Figure 7. Distribution of our sample in the offset velocity-EW plane. C IV and He II share similarly shaped two-dimensional distributions.

because, similar to those of C IV, sources with extreme He II blueshifts also tend to have small EWs. Instead, these similarities suggest that the blueshifts of He II and C IV share the same physical origin, and the blueshift might be a common feature of all high-ionization emission lines.

C IV EW correlates well with both Mg II EW and He II EW (left panels of Figure 8). As a result, both Mg II EW and He II EW are correlated with the C IV blueshift. Meanwhile, the difference between C IV and Mg II EWs and the C IV blueshift are anti-correlated (the lower right panel of Figure 8). Such anti-correlation is also obtained between Hβ and C IV (Sulentic et al. 2017). A similar anti-correlation is not evident for C IV and He II (the upper right panel of Figure 8). Compared with Mg II (whose ionization energy is $\sim$10 eV), the ionization energy of high-ionization BELs (e.g., C IV or He II) is much higher (i.e., $\sim$50 eV). The ratio of the flux of a BEL to that of quasar continuum at the ionization energy measures the covering factor of the BLR gas. If the ratio of the covering factor of Mg II to that of C IV (or He II) is independent of the C IV blueshift, our results indicate that, with the presence of a

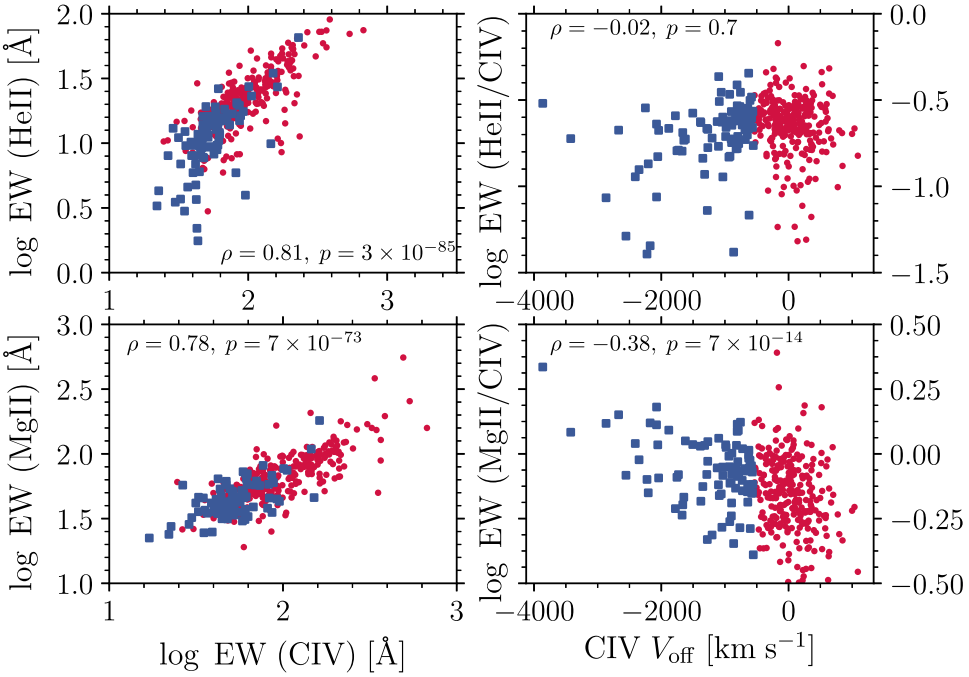

Figure 8. Upper left: He II EW as a function of C IV EW. Upper right: logEW(HeII) − logEW(CIV) as a function of the C IV blueshift. Lower panels: the same as the upper panels, but for Mg II. In each panel, the high-blueshift sources are highlighted as blue squares, and the correlation between the x-axis and y-axis variables is evaluated via the Spearman rank correlation (i.e., Spearman's ρ). It appears that, in the presence of a large C IV blueshift, C IV and He II are preferentially suppressed with respect to Mg II.

large C IV blueshift, the high-energy ($E \sim 50$ eV) ionizing continuum is preferentially reduced with respect to the lower-energy ($E \sim 10$ eV) one.

3.2. The Blueshift and Line Widths

Previous works (e.g., Sulentic et al. 2007; Shen & Liu 2012; Runnoe et al. 2013; Brotherton et al. 2015; Coatman et al. 2016, 2017) often argue that, unlike low-ionization emission lines (e.g., Hβ, Mg II), C IV is a biased estimator of $M_{\rm BH}$. Notably, there is an anti-correlation between $\rm FWHM_{C\,IV}/FWHM_{MgII}$ and the C IV blueshift (see, e.g., Shen et al. 2008). We also used our data to explore this anti-correlation since our coadded data do not suffer from short-timescale (i.e., rest-frame ∼60 days) quasar variability. We confirm an anti-correlation between $\rm FWHM_{C\,IV}/FWHM_{MgII}$ and the C IV blueshift (Figure 9), indicating that Mg II- and C IV-based $M_{\rm BH}$ will be inconsistent. Similar relations are also observed between the ratio of the line dispersion $\sigma_{\rm C\,IV}/\sigma_{\rm Mg\,II}$ and the C IV blueshift (Figure 10).

These results suggest that, in the presence of the C IV blueshift, both $\rm FWHM_{C\,IV}$ and $\sigma_{\rm C\,IV}$ are biased, and corrections are required. Unlike FWHM, the line dispersion σ is more sensitive to the wings of the line profile. The correction for $\sigma_{\rm C\,IV}$ is much smaller than that for $\rm FWHM_{C\,IV}$. Therefore, the core of the C IV profile is preferentially "broadened" as a function of the C IV blueshift. This result also indicates that σ is a more reliable estimator of the virial motions. In practice, we prefer to estimate $M_{\rm BH}$ by making empirical corrections to $\rm FWHM_{C\,IV}$ (see also Coatman et al. 2017). The proposed approach has two advantages. First, FWHM is better constrained than σ in low S/N spectra. Second, for extreme blueshift sources, there is no clear correlation between σ and the blueshift.

The slope of our anti-correlation between the ratio of $\rm FWHM_{C\,IV}$ to $\rm FWHM_{MgII}$ and the C IV blueshift is consistent

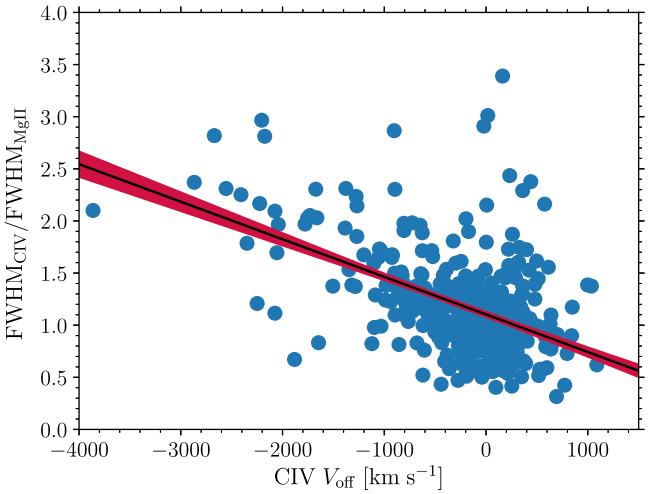

Figure 9. Following Coatman et al. (2017), we fit $\rm FWHM_{C\,IV}/FWHM_{Mg\,II}$ as a function of the C IV blueshifts. The best-fit relation (via the Bayesian linear regression method; see Kelly (2007) is $y = (-0.36 \pm 0.03)x + (1.1 \pm 0.02)$ with an intrinsic scatter of 0.41 ± 0.02, where $x = V_{\rm off}/10^3$ km s^{-1}.

with the correlation between C IV and Hβ found by Coatman et al. (2017). The intercept and the intrinsic scatter of our relation are larger than those of Coatman et al. (2017) by a factor of two. The differences could be caused by the imperfect one-to-one relation between $\rm FWHM_{MgII}$ and $\rm FWHM_{H\beta}$ (Trakhtenbrot & Netzer 2012) or the differences in how we estimate C IV blueshift compared with Coatman et al. (2017).

The shape of C IV, $D_{\rm C\,IV}$ (for its definition, see Section 2.2), is also expected to be anti-correlated with the C IV blueshift since the corrections for FWHM and σ are different. This speculation is confirmed by the Spearman rank correlation ($\rho = -0.13$, and $p = 0.008$; see Figure 11), albeit with a substantial scatter. In other words, the high-blueshift sources

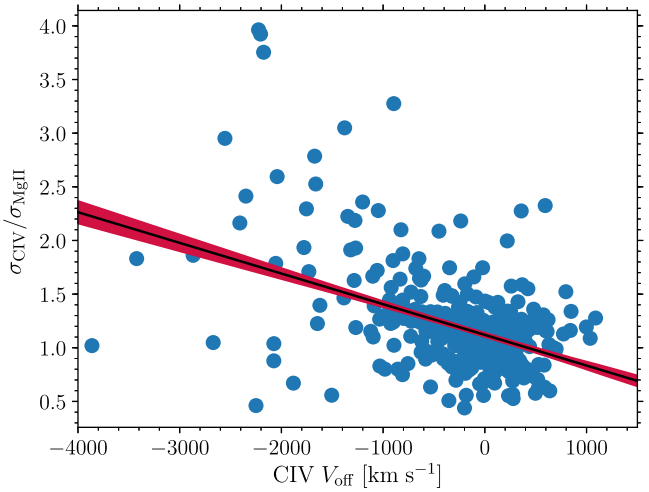

Figure 10. Behavior of $\sigma_{\rm C\,IV}/\sigma_{\rm Mg\,II}$ as a function of the C IV blueshifts. The best-fit relation is $y = (-0.28 \pm 0.03)x + (1.12 \pm 0.02)$ with an intrinsic scatter of 0.34 ± 0.02. For the extreme blueshift sources, there is no clear correlation between $\sigma_{\rm C\,IV}/\sigma_{\rm Mg\,II}$ and the C IV blueshift. This result, along with Figure 9, suggests that, for wind dominated sources, the core of the C IV profile is preferentially "broadened."

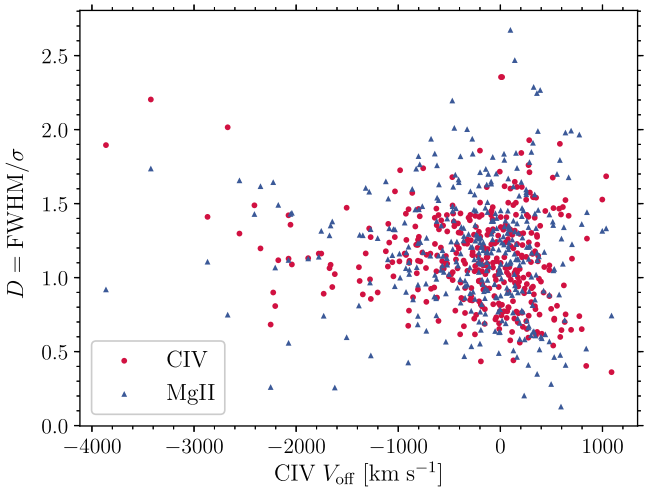

Figure 11. Behavior of the line shape D as a function of the C IV blueshifts. For C IV, there is a weak anti-correlation between $D_{\rm C\,IV}$ and the C IV blueshifts ($\rho = -0.13$ and $p = 0.008$). However, there is no anti-correlation between $D_{\rm Mg\,II}$ and the C IV blueshifts ($\rho = -0.07$ and $p = 0.1$).

tend to avoid the small $D_{\rm C\,IV}$ (i.e., more boxy) space. Therefore, like the C IV blueshift, $D_{\rm C\,IV}$ can also be adopted as a viable and practical proxy to correct FWHM$_{\rm C\,IV}$ (Denney 2012), although the correction may be inadequate at extreme C IV blueshift. There are two possible explanations for the anti-correlation. First, the spectra of the low-blueshift sources have significant narrow C IV components. The contribution of the narrow C IV component to the total flux is smaller for the high-blueshift sources. If this scenario is correct, we would expect the shape of Mg II to show the same anti-correlation. However, we found that, according to the Spearman rank correlation test, there is no significant correlation between the shape of Mg II and the C IV blueshift ($\rho = -0.07$ and $p = 0.1$; see Figure 11). Second, there is an intrinsic anti-correlation between the shape of C IV and its blueshift. This anti-correlation seems to be inconsistent with the scenario proposed by Gaskell (2009) in which the line profiles of high-blueshift sources are expected to be less boxy (i.e., have smaller values of $D_{\rm C\,IV}$).

4. Variability of the Line Shift

We can also study the C IV blueshift for each of the 29 epochs. The intrinsic variability of the blueshift of C IV can be constrained by calculating the "excess of variance" (see, e.g., Sun et al. 2015),

$$\mathrm{VAR.}(V_{\rm shift,se}) = \sqrt{(0.74\mathrm{IQR}(V_{\rm shift,se}))^2 - \widetilde{V^2}_{\rm err}}\,, \qquad (1)$$

where IQR($V_{\rm shift,se}$) and $V_{\rm err}$ are the 25%–75% interquartile range and the uncertainty of $V_{\rm shift,se}$, respectively. $\widetilde{V}^2_{\rm err}$ represents the median value of the variable $V^2_{\rm err}$.

The dynamical timescale of the BLR is

$$T_{\rm dyn} \sim \frac{2\pi}{\Omega_{\rm K}} = 253\left(\frac{R_{\rm BLR}}{10^3 R_{\rm S}}\right)^{3/2}\frac{M_{\rm BH}}{5\times10^7 M_\odot}\ \mathrm{days}, \qquad (2)$$

where $\Omega_{\rm K}$, $R_{\rm BLR}$, and $R_{\rm S}$ are the Keplerian angular velocity, the radial distance of the BLR to the SMBH, and the Schwarzschild radius, respectively. With the timescales we consider here (i.e., $\lesssim$60 rest-frame days, which are much smaller than $T_{\rm dyn}$), the variability is likely driven by the quasar continuum variations. For instance, let us consider that the time lags between the ionizing continuum and the BELs depend on the line-of-sight velocities (see, e.g., Denney et al. 2009; Grier et al. 2013). The time lags of the blue and red wings will be different. If the time lag of the blue wing is shorter than the red wing, as the quasar continuum increases (decreases), we will observe a quick response of the blue wing, i.e., an apparent blueshift (redshift) until the red wing responds to the increase (decrease) at a later epoch. Therefore, being either blueshifted or redshifted, and the variations on short timescales are expected (hereafter, the "line-of-sight velocity-dependent reverberation"; see Barth et al. 2015).

4.1. The Line Shift of Mg II

To understand the line-shift variations due to reverberation, we first study Mg II. The upper panel of Figure 12 illustrates the distribution of the variability of the line shift of Mg II (VAR.($V_{\rm shift,Mg\,II,\ se}$)) for our three subsamples. Note that the uncertainty of VAR.($V_{\rm shift,Mg\,II,\ se}$) is generally not small for each source. Hence, we focus only on the median VAR.($V_{\rm shift,Mg\,II,\ se}$) of each subsample. Meanwhile, we have visually inspected those sources that show very large VAR.($V_{\rm shift,Mg\,II,\ se}$) (i.e., $\gg$300 km s^{-1}) and found that, in many cases, their single-epoch spectra are noisy and the best-fitting results are not robust. Therefore, we rejected these sources.

To better control the effect of EW(C IV), we created control samples matched in EW(C IV), $L1350$, and redshift. More specifically, for each source in Sample A (i.e., the "high-blueshift, small-EW" sample), we randomly (with replacement) selected a quasar from the sources in Samples B or C with similar C IV EW (within 0.1 dex). We then adopt the Anderson–Darling test[18] to measure the probability that the randomly selected sample is drawn from the same parent population as sample A in terms of C IV EW, $L1350$, and redshift. The two samples are consistent

[18] The Anderson–Darling test is found to be more sensitive at recognizing the difference between two distributions than the popular Kolmogorov–Smirnov test (e.g., Hou et al. 2009).

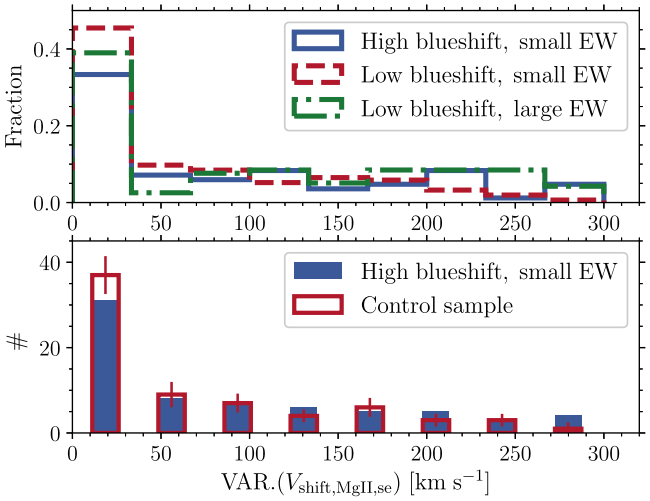

Figure 12. Upper panel: distributions of the intrinsic variability of $V_{\rm shift,Mg\ II,\ se}$ for three different subsamples. Most sources show weak variability of $V_{\rm shift,Mg\ II,\ se}$. Lower panel: a comparison between the distribution of the Mg II line shift variations of sample A sources (i.e., the "high-blueshift, small-EW" sources) to that of the "controlled sample" (matched in C IV EW, $L1350$, and redshift). The median VAR.($V_{\rm shift,Mg\ II,\ se}$) of extreme blueshift sources is larger than that of the control sample.

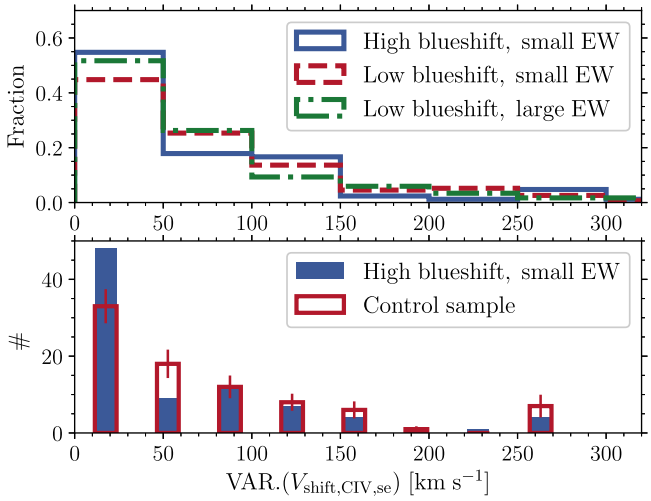

Figure 13. Upper panel: distributions of the intrinsic variability of $V_{\rm shift,\ C\ IV,\ se}$ for three different subsamples. Similar to that of Mg II, most sources show weak variability of $V_{\rm shift,C\ IV,se}$. Lower panel: a comparison between the distribution of the C IV line shift variations of sample A sources (i.e., the "high blueshift, small EW" sources) and that of the "controlled sample" (matched in C IV EW, $L1350$, and redshift). The high-blueshift sources have smaller median VAR.($V_{\rm shift,C\ IV,se}$), opposite to what is observed for Mg II.

with being matched if the null-hypothesis probability $p > 0.05$. We then calculate the distributions of VAR.($V_{\rm shift,Mg\ II,\ se}$) for sample A and the control sample. We repeated this procedure 1024 times. Our results are presented in the lower panel of Figure 12. The median VAR.($V_{\rm shift,Mg\ II,\ se}$) of sample A is 56.4 ± 8.9 km s^{-1}, whereas, the median VAR.($V_{\rm shift,Mg\ II,\ se}$) of the control sample is 33.1 ± 16.5 km s^{-1}.[19] Of our 1024 realizations, the possibility to have VAR.($V_{\rm shift,Mg\ II,\ se}$) $\geqslant 56.4$ km s^{-1} is less than 3%. We thus conclude that VAR.($V_{\rm shift,Mg\ II,\ se}$) of sample A is statistically larger than that of the control sample.

4.2. The Line Shift of C IV

In this section, we check the variability properties of the C IV blueshift with respect to the coadded high S/N Mg II. Therefore, the variations presented in this section are only due to the line shift of C IV. As in Section 4.1, we focus only on the median VAR.($V_{\rm shift,C\ IV,\ se}$), discarding sources with VAR.($V_{\rm shift,C\ IV,\ se}$) > 300 km s^{-1}.

Figure 13 shows the results of the analysis of VAR.($V_{\rm shift,C\ IV,\ se}$). The median VAR.($V_{\rm shift,C\ IV,\ se}$) of Sample A (i.e., the "high blueshift, small EW" sample) is 11.6 ± 4.5 km s^{-1}. For the control sample, the median VAR.($V_{\rm shift,C\ IV,\ se}$) is 58.7 ± 8.7 km s^{-1}. Of our 1024 realizations, none has VAR.($V_{\rm shift,C\ IV,\ se}$) $\leqslant 11.6$ km s^{-1}. Therefore, contrary to the results for Mg II, sample A sources have slightly weaker C IV line shift variability than that of the control sample. Meanwhile, the line shift of Mg II varies more strongly than that of C IV. Indeed, the Mann–Whitney U test[20] of the line-shift variability on Mg II and C IV indicates that the variation amplitude of Mg II is statistically larger than that of C IV (the p-value is 0.003). These differences indicate that the structure of C IV evolves as a function of the C IV blueshift in a way that is different from that of Mg II.

[19] The uncertainty is the dispersion of the 1024 realizations.

[20] The Mann–Whitney test is a nonparametric test of the null hypothesis that the distributions of two populations are equal.

In the high-redshift universe, broad Mg II or C IV lines are sometimes adopted to determine the quasar redshift. As discussed by Denney et al. (2016, 2016) and Shen et al. (2016), such redshift estimation is significantly biased, depending on quasar properties. The bias can be corrected to be better than $\sim$200 km s^{-1} by some empirical guidelines (Shen et al. 2016). However, our results (Figures 12 and 13) indicate that quasar variability places lower limits on the accuracy of measuring quasar redshifts with only single-epoch BELs. For some sources, the accuracy can be worse than 200 km s^{-1}.

5. Discussion

5.1. C IV Blueshift and Quasar Variability

Our analyses in Section 4 demonstrate that the observed C IV blueshift can vary due to line-of-sight velocity-dependent reverberation. Therefore, quasar variability might have effects on the C IV EW-offset velocity connection.

Let us first determine how much quasars can move in the C IV EW-offset velocity plane due to quasar variability. To do so, we selected three sources, i.e., one from sample A, one from sample B, and one from sample C. The selection criteria are as follows. For each sample, we selected the source with the highest ratio of the VAR.($V_{\rm shift,C\ IV,\ se}$) to the median measurement error of C IV $V_{\rm shift,C\ IV,\ se}$ such that VAR.($V_{\rm shift,C\ IV,\ se}$) is the most robust one. Figure 14 presents our results. For the three selected sources, $\sim$20% of their motions along the C IV blueshift are due to measurement uncertainties. These sources do not rapidly change their positions over the time period of our observations (see also Figure 13).

We then explored the possible correlation between $V_{\rm off,se}$ and EW over the 29 epochs for each source. Figure 15 presents the distributions of the Spearman rank correlation coefficient ρ. For most of our sources, the correlation is statistically insignificant. This result is not totally unexpected as the timescale of our multi-epoch data is short ($\sim$60 days) and quasar variability is weak on short timescales. However, on average, $V_{\rm off,se}$ and EW

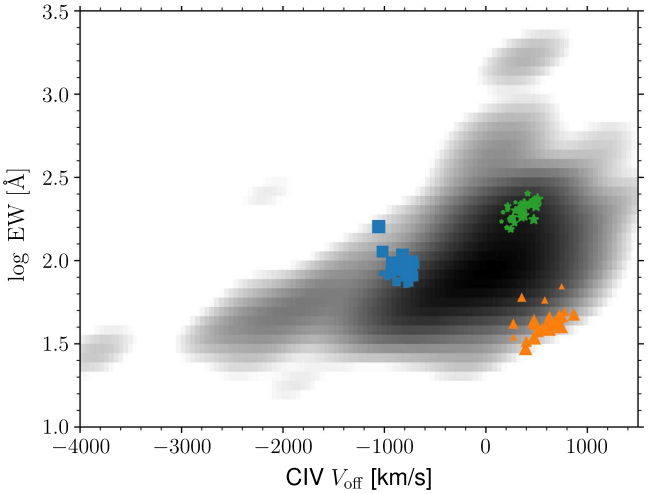

Figure 14. Locations of three sources in the C IV EW-offset velocity plane. The three sources are selected from sample A (blue squares), sample B (orange triangles), and sample C (green stars), respectively. For each source, the symbol size increases with time. The gray color indicates the probability density distribution of our whole sample. Consistent with Figure 13, sources do not strongly change their positions. Refer to the animation to witness the locations of the three sources over time.

(An animation of this figure is available.)

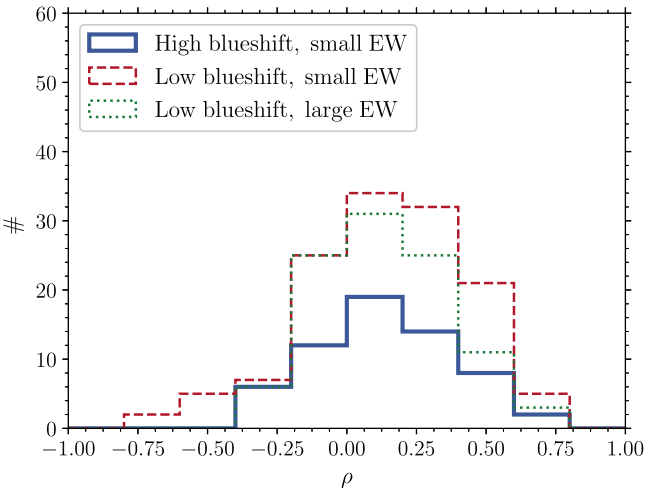

Figure 15. Distributions of the Spearman rank correlation coefficient ρ between $V_{\rm off,\ se}$ and EW over the 29 epochs. There is, on average, a positive correlation between $V_{\rm off,\ se}$ and EW, which is consistent with the global C IV EW-offset connection.

are positively correlated over the 29 epochs. We further examined the 36 sources with statistically significant correlations and found that only 4 of them have negative correlations (0/5, 4/22, and 0/9 for samples A, B, and C, respectively). In Figures 16–18, we illustrate the single-epoch C IV EW as a function of $V_{\rm off,se}$ for these 36 sources. Most of their motions along the C IV EW are due to random fluctuations that are driven by the measurement uncertainties.

In Figures 19–21, we show three examples of the variations of the C IV profile. As an aid to visual inspection, for each source, we divided its 29 observations into three groups according to the increasing single-epoch C IV EW (i.e., the 29 observations are sorted by the single-epoch C IV EW; the 1st–9th, 10th–19th, and 20th–29th reordered observations belong to Groups 1, 2, and 3, respectively); for each group, we created

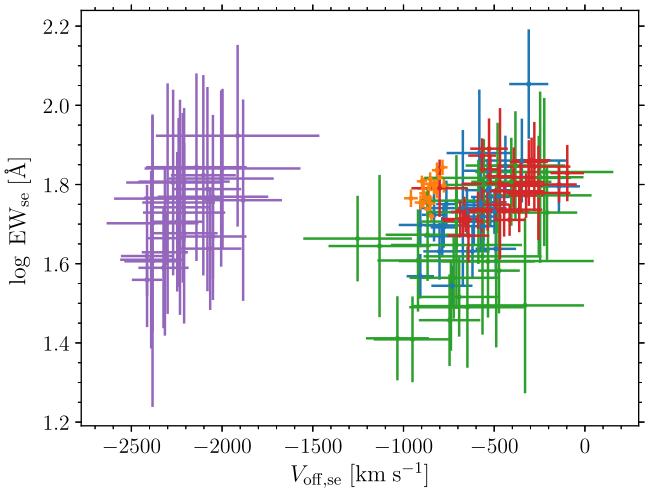

Figure 16. Single-epoch C IV EW as a function of $V_{\rm off,\ se}$ for the five sources in sample A (i.e., the "high-blueshift, small-EW" sample). For these sources, there are statistically significant positive correlations between the single-epoch C IV EW and $V_{\rm off,\ se}$.

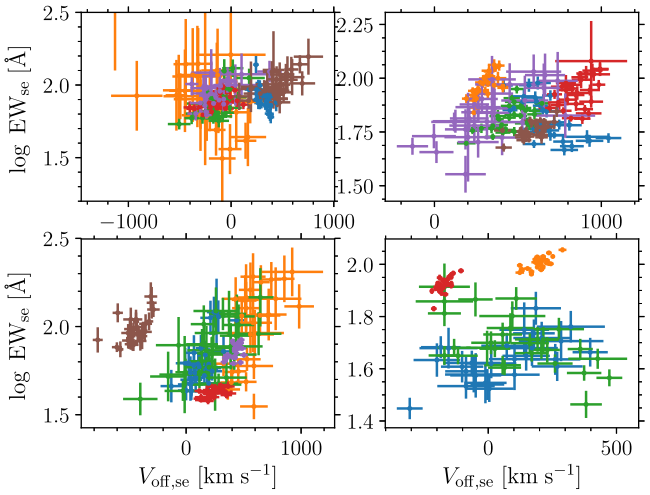

Figure 17. Single-epoch C IV EW as a function of $V_{\rm off,\ se}$ for the 22 sources in sample B (the "low-blueshift, small-EW" sample). For these sources, there are statistically significant positive (18 sources) or negative (4 sources) correlations between the single-epoch C IV EW and $V_{\rm off,\ se}$. To avoid severe overlapping and confusion, the 22 sources spread across four panels. The upper and lower left panels each contain six sources; the lower right panel contains four sources.

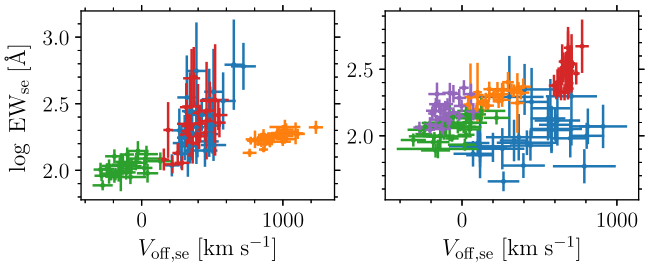

Figure 18. Single-epoch C IV EW as a function of $V_{\rm off,\ se}$ for the nine sources in sample C (the "low-blueshift, large-EW" sample). For these sources, there are statistically significant positive correlations between the single-epoch C IV EW and $V_{\rm off,\ se}$. To avoid severe overlapping and confusion, the nine sources spread across two panels. The left (right) panel contains five (four) sources.

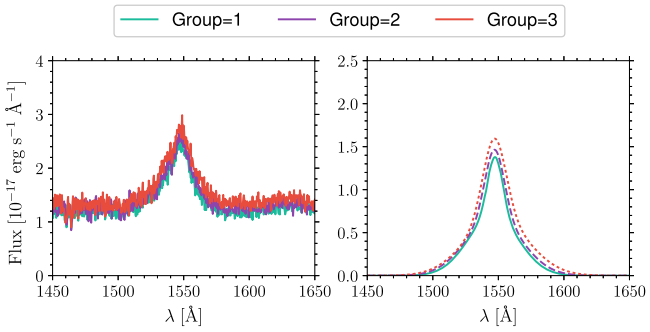

Figure 19. Time evolution of the C IV profile for a sample A QSO (RMID = 108). The left and right panels represent the high S/N mean spectrum in each group (for its definition, see the text for more details) and the best fits of C IV. The spectra and the best fits of C IV profiles are normalized to the best-fitting 1550 Å continuum. In this example, groups with higher C IV EW tend to be less blueshifted.

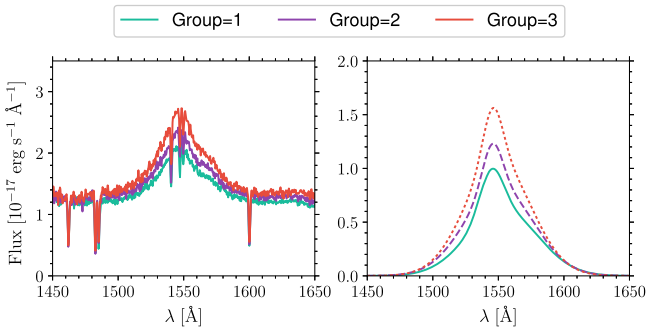

Figure 20. Time evolution of the C IV profile for a sample B QSO (RMID = 231). The left and right panels represent the high S/N mean spectrum in each group (for its definition, see the text for more details) and the best fits of C IV. The spectra and the best fits of C IV profiles are normalized to the best-fitting 1550 Å continuum. In this example, groups with higher C IV EW tend to be more blueshifted.

the variance-weighted high S/N mean spectrum; we fitted the mean spectra following the spectra-fitting approach mentioned in Section 2.1. When being plotted, all spectra and best fits of C IV profiles are normalized to the best-fitting 1550 Å continuum. Therefore, the intensities of C IV in the figures are proportional to their EWs.

The positive correlation between C IV EW and offset velocity could be induced by some bias in our spectral fitting procedure. As mentioned in Section 2.1.2, we only fit C IV in [1500 Å, 1600 Å] for single epoch spectra. It is possible that our code interprets weak He II as the red wing of C IV. As a result, we would expect an artificial positive correlation between C IV EW and offset velocity. We therefore performed a simple simulation to account for this bias. We selected RMID = 693 as an example.[21] A total of 29 mock spectra were generated, where the flux in each wavelength pixel was determined by adding the single-epoch flux density noise to the best-fit model of the composite spectrum. We then fitted the mock spectra following the same fitting recipe. We find that the variability in the mock spectra is mostly due to measurement errors and the variability amplitude is much less than the true single-epoch spectra. In addition, for the mock spectra, the correlation between C IV EW and offset velocity is statistically insignificant. We therefore conclude that the bias we

[21] We chose this source because the boundary between C IV and He II is not visually evident in its composite spectrum. Therefore, the bias can be large. We also tested some other sources and found similar results.

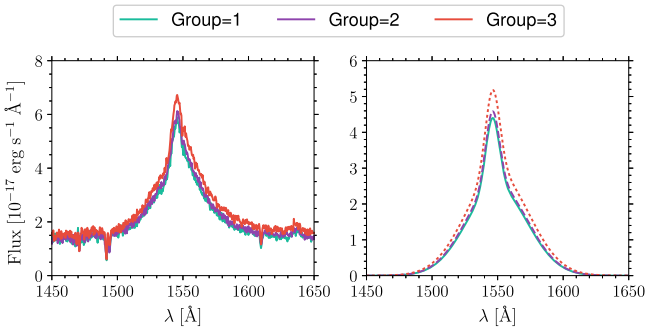

Figure 21. Time evolution of the C IV profile for a sample C QSO (RMID = 491). The left and right panels represent the high S/N mean spectrum in each group (for its definition, see the text for more details) and the best fits of C IV. The spectra and the best fits of C IV profiles are normalized to the best-fitting 1550 Å continuum. In this example, groups with higher C IV EW tend to be less blueshifted.

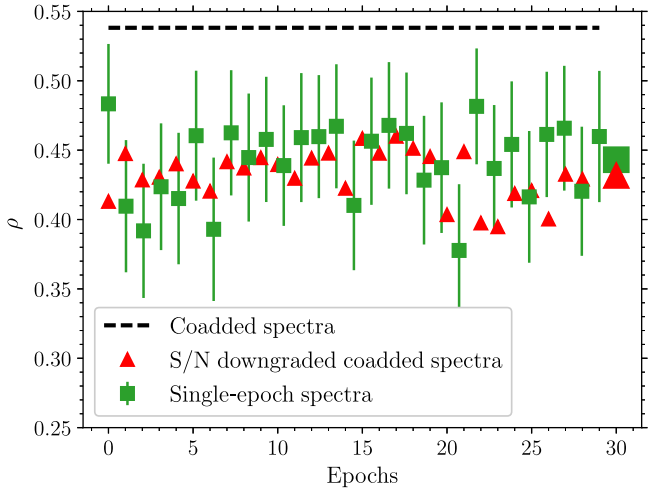

Figure 22. Spearman rank correlation coefficient, ρ, between the C IV EW and offset velocity for each epoch (small green squares). The black dashed line corresponds to the measurements of the high S/N composite spectra. Small red triangles are for the measurements of the composite spectra with downgraded S/N (i.e., matched in the S/N of each single-epoch measurements). The large red triangle and the large green square represent the mean correlation coefficient for the S/N downgraded composite data and the single-epoch data, respectively. The green squares are, on average, above the red triangles, which indicates that the correlation is slightly tighter for the single-epoch data. That is, quasar variability can enhance the connection between the C IV EW and offset velocity.

mentioned cannot be responsible for the observed positive correlation.

How do we understand these statistically significant positive or negative correlations? As we mentioned in Section 4, the observed line-shift variations are likely driven by the "line-of-sight velocity-dependent reverberation." Meanwhile, as revealed by many multi-wavelength variability studies, quasars tend to be bluer when they become brighter (e.g., Giveon et al. 1999; Vanden Berk et al. 2004; Guo & Gu 2016) and such a behavior is more prominent on short timescales (∼10 days, see Sun et al. 2014; Zhu et al. 2016). Let us again assume that the time lag of the blue part is shorter than that of the red one. As the quasar continuum increases (decreases), the blue wing will respond faster than the red wing, which results in an apparent blueshift (redshift); we will observe a harder (softer) quasar SED, i.e., a larger (smaller) EW. Therefore, these positive or negative correlations might be driven by the dependency of the BEL time lag on the line-of-sight velocity and the color variability of quasars.

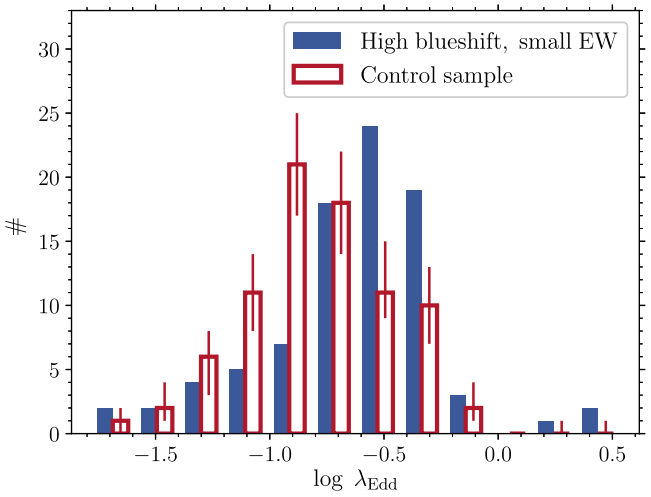

Figure 23. Distributions of the Eddington ratio, λ_{Edd}. Filled blue bars represent sample A sources (the "high-blueshift, small-EW" sources). Open red bars with errors represent the control sample (matched in C IV EW, $L1350$, and redshift). The extreme blueshift sources tend to have large Eddington ratios.

The overall positive correlation is consistent with the global C IV EW-offset velocity connection (i.e., sources with strong C IV tend to be less blueshifted; see, e.g., Figure 4). As a result, we expect that quasar variability acts in such a way to enhance the global C IV EW-offset velocity connection. Compared with the single-epoch data, our high S/N composite spectra do not suffer from short-timescale (~60 rest-frame days) variability. Therefore, we can assess the effect of quasar variability by comparing the scatter of the C IV EW-offset velocity connection of the composite spectra with that of the single-epoch data. We first added random noise to the C IV EW and V_{off} (i.e., measurements from the composite spectra) such that their S/Ns are identical to those of the C IV EW_{se} and $V_{off,se}$ (i.e., measurements from the single-epoch spectra). The C IV velocity offset for each epoch we adopted here is with respect to the composite Mg II profile (i.e., $V_{off,se}$). We adopted this definition to focus on the variability of C IV alone. We then calculated Spearman's ρ between the C IV EW-offset velocity for the S/N downgraded composite data; Figure 22 presents our results. The exact value of ρ depends on epochs since the S/N of spectra changes with epochs. We also obtained the median ρ over the 29 epochs. The differences between the correlation coefficient of the S/N downgraded composite data and that of the single-epoch data are due to quasar variability. The median ρ of the single-epoch spectra is slightly larger (by 2.5%) than that of the S/N downgraded composite data. Our results indicate that quasar variability might slightly enhance the connection between the C IV EW-offset velocity.

5.2. The Physical Origin of the C IV Blueshift

It remains unclear why sources with blueshift tend to have low EW, but many other low EW quasars do not have a blueshift. We compare these two types of sources in terms of other quasar properties, especially the Eddington ratio, as there are suggestions that the C IV EW is tightly correlated with the Eddington ratio (e.g., Bachev et al. 2004; Baskin & Laor 2004; Shemmer & Lieber 2015). To reduce effects caused by other factors, for Sample A (sources with low EW and high blueshift), we again made control samples matched in the C IV EW, $L1350$, and redshift. Our results are presented in Figure 23. While the median logarithmic Eddington ratio of sample A is −0.6, the median logarithmic Eddington ratio of the control sample is -0.86 ± 0.04. Therefore, after controlling for the C IV EW, quasar luminosity, and redshift, the C IV blueshift sources tend to have significantly larger (~0.3 dex) Eddington ratios.

There are two simple scenarios that can explain this result. First, the observed correlation is simply an orientation effect (Denney 2012). In this scenario, the high- and low-blueshift sources might intrinsically have similar Eddington ratios. However, the high-blueshift sources are viewed more face on. When being viewed face on, the geometrically thin accretion disk will be more luminous than the edge-on case. In addition, the face-on systems suffer less from absorption (due to, e.g., a torus) than the edge-on ones. For a polar wind, the line-of-sight blueshift velocity would be higher for the face-on case. As a result, the extreme blueshift sources apparently have larger Eddington ratios than the low blueshift counterparts. This scenario is, however, challenged by some recent observations. For instance, Runnoe et al. (2014) measured orientation for a quasar sample via the radio core dominance parameter; they found that there is no correlation between the C IV blueshift and orientation. Second, the C IV blueshift sources are intrinsically more active, i.e., the high-blueshift sources have larger Eddington ratios than those of the low-blueshift sources. These two scenarios can be further tested by exploring the variability of the quasar continuum. The variability of the quasar optical/UV continuum is observed to be anti-correlated with the Eddington ratio (e.g., Ai et al. 2010; MacLeod et al. 2010; Kelly et al. 2013; Kozłowski 2016; Rumbaugh et al. 2017), after controlling for quasar luminosity, and redshift. Therefore, according to the first scenario, the high- and low-blueshift sources share similar variations of the quasar continuum; however, the variability amplitude of the quasar continuum for the high-blueshift sources would be smaller than the low-blueshift ones in the second scenario.

We then calculated the r-band intrinsic variability[22] for sample A and the corresponding control sample. We first calculated the synthetic flux in the r band by convolving the r-band bandpass with the spectra. As a second step, we calculated the structure function (we adopted the IQR estimator; see, e.g., Sun et al. 2015) for sample A and the control sample. Our results are presented in Figure 24. It is clear that sources in sample A are intrinsically less variable. Therefore, our results disfavor the orientation scenario, but support the idea that high-blueshift sources are often more active (i.e., have higher Eddington ratios). Luo et al. (2015) explored the X-ray properties of PHL 1811 analogs and weak-line quasars that also show evident C IV blueshifts. They found that these sources tend to suffer from significant (intrinsic) X-ray absorption. They proposed that PHL 1811 analogs and weak-line quasars can be well explained if these sources have very large Eddington ratios, which appears to be in line with our Eddington-ratio scenario.

As the accretion rate increases, the temperature of the accretion disk increases, which produces more UV photons. Meanwhile, as revealed by recent radiation magnetohydrodynamic simulations (e.g., Jiang et al. 2014a), the energy dissipation efficiency of the X-ray corona decreases with the accretion rate. The X-ray corona will be more efficiently cooled due to inverse Compton scattering of these UV photons, i.e.,

[22] We chose this band because the corresponding wavelength is around ~6000 Å, which has the smallest spectrophotometric uncertainty (Sun et al. 2015).

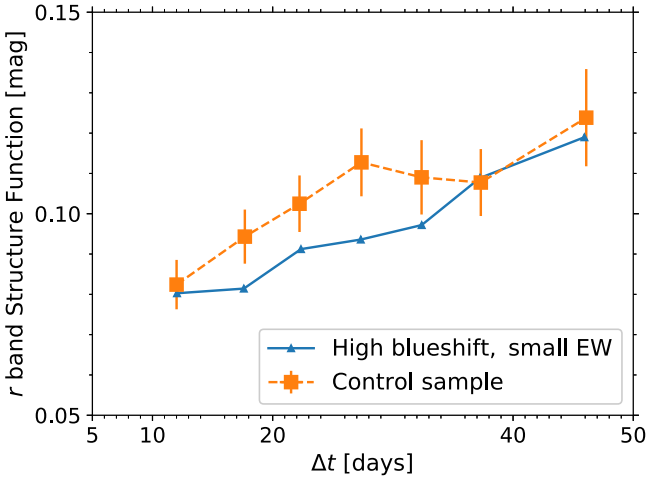

Figure 24. The *r*-band variability amplitude as a function of the rest-frame time interval, Δt. Sample A sources (the "high-blueshift, small-EW" sources) are less variable, indicating higher Eddington ratios. As reported by Sun et al. (2015), the variability estimation on timescales <10 days are biased; we therefore only consider quasar variability on longer timescales.

the SED becomes softer (i.e., having larger α_{ox}) with the increasing Eddington ratio. In addition, the inner accretion disk is puffed up at high Eddington ratios (e.g., $\lambda_{Edd} \gtrsim 0.3$) due to radiation pressure (e.g., Abramowicz et al. 1988; Wang & Netzer 2003; Jiang et al. 2014b; Sądowski et al. 2014). The puffed-up disk could act as a "shielding" gas (e.g., Leighly 2004; Wu et al. 2011; Luo et al. 2015) that blocks both the X-ray coronal emission and the ionizing continuum, i.e., the SED is expected to be softer. Quasars with such softer SEDs (i.e., weaker X-ray emission) can launch strong winds from the accretion disk (e.g., Murray & Chiang 1997; Leighly 2004; Richards et al. 2011; Chajet & Hall 2013, 2017; Luo et al. 2014).

The Eddington-ratio scenario has important implications for RM. According to the SED-evolution picture, the radius-optical luminosity relation of the low-blueshift sources is invalid for the high-blueshift ones; in those cases, the radius and M_{BH} will be overestimated. Therefore, for the high-blueshift sources, the Eddington ratios we measured (for the methodology, see Section 2.2) might be lower limits on the true values. A direct test can be applied to our scenario by performing RM campaigns (e.g., SDSS-RM; Shen et al. 2015) for the extreme blueshift sources, and exploring the radius-optical luminosity relation as a function of the C IV blueshift (also see Richards et al. 2011).

5.3. The Connection between the C IV Blueshift and Quasar Properties

This Eddington-ratio scenario can also explain additional observational results in this work. According to our scenario, when the Eddington ratio increases, the SED becomes softer and the covering factor of the shielding gas to the BLR increases (Luo et al. 2015). Hence, we expect the BELs to be weaker. C IV and He II (or other high-ionization lines) would be preferentially reduced with respect to Mg II (or other low-ionization lines) as the ionization energy of the former is larger. Therefore, the Eddington-ratio scenario can plausibly explain our results in Figure 8.

How do we explain the fact that FWHM and σ are both anti-correlated with the blueshifts (Figures 9 and 10)? This relation is apparently inconsistent with previous results from Denney (2012), who found that the rms spectra of C IV (which are assumed to represent the variable emissions) are broader than the mean spectra, indicating that the non-variable blueshift component should be narrower than the "canonical" (or disk) C IV profile. As pointed out by Barth et al. (2015), rms spectra only evaluate the relative variability amplitude as a function of the line-of-sight velocity. It is possible to produce very broad rms spectra (broader than the single-epoch disk profile) if the high line-of-sight velocity gas responds more efficiently than that of the low line-of-sight velocity gas. However, as high velocity components are generally produced in the high-ionization region, it is unlikely that this emission is more sensitive to the continuum variations (Korista & Goad 2004). The Eddington-ratio scenario could provide a plausible explanation for why the ratio of the line width (measured as both FWHM and σ) of C IV to that of Mg II increases with the C IV blueshift. The radius of the BLR gas should scale as $L_{ion}^{0.5}$, where L_{ion} is the ionizing continuum luminosity. The ratio of the C IV radius to that of Mg II decreases with the increasing Eddington ratio. Therefore, $FWHM_{C\,IV}/FWHM_{MgII}$ and $\sigma_{C\,IV}/\sigma_{Mg\,II}$ are expected to be correlated with the C IV blueshift. The accretion-disk winds may produce singly peaked (which is due to the radiative-transfer effects, e.g., the escape probability is anisotropic; see Murray & Chiang 1997) and boxy (i.e., large values of D) C IV profiles since they are generated in the inner high-speed regions. Therefore, the line profiles of high-blueshift sources are more boxy (i.e., large values of D) than those of the low-blueshift ones. It is also conceivable that, as the Eddington ratio increases, the radiation pressure plays a more important role in accelerating clouds (especially low column density ones; see, e.g., Marziani et al. 2010). Such clouds could produce blueshifted broad C IV. This mechanism could also be (at least partially) responsible for the observed anti-correlation between the line-width ratio and the C IV blueshift.

A remaining question is why quasars with different Eddington ratios/SEDs can have similar C IV EWs. Previous works suggest that the "Baldwin effect" might be induced by the tight correlation between EWs and the Eddington ratios (e.g., Bachev et al. 2004; Baskin & Laor 2004; Shemmer & Lieber 2015). However, the C IV or He II EW measures only the ratio of the product of the $E_{ion} \gtrsim 50$ eV extreme UV (EUV) emission and the effective covering factor of the BLR clouds to $L1350$. It is possible that either $L1350$ or EUV emission cannot effectively track the disk emission (also see Vasudevan & Fabian 2007) and/or the effective covering factor varies among quasars. Therefore, the C IV or He II EW is not an accurate indicator of the Eddington ratio or quasar SED.

5.4. The Evolution of the Line-shift Variability

How do we understand the evolution of the line-shift variability as a function of the C IV blueshift? Recall that the observed line-shift variations are driven by the "line-of-sight velocity-dependent reverberation" (see the first paragraph of Section 4). According to this scenario, the variability amplitude depends on the time-lag difference between the blue and red wings and on the variations of the ionizing continuum. The time-lag difference is expected if the BLR gas has significant radial motions (see also Barth et al. 2015).

The line-shift variability of Mg II is more extreme than that of C IV. At a first glance, this result is not expected since the

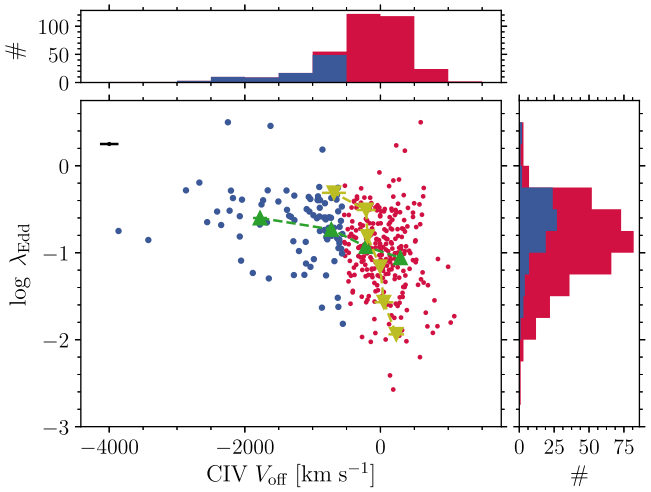

Figure 25. Distribution of our sample in the C IV offset velocity-$\lambda_{\rm Edd}$ plane. Sources with offset velocity < -550 km s^{-1} are highlighted by blue colors. The green (yellow) triangles represent the mean log $\lambda_{\rm Edd}$ (C IV $V_{\rm off}$) in each C IV $V_{\rm off}$ (log $\lambda_{\rm Edd}$) bin. Large blueshift velocities tend to correspond to large $\lambda_{\rm Edd}$. However, the reverse is not true.

ionization energy of C IV is much larger than that of Mg II, and the variability amplitude of quasar continuum emission generally increases with energy. We argue that our result could be explained as follows. The distance of the location of the Mg II gas should be larger than that of C IV, suggesting that the Mg II gas is radially more extended. As a result, the Mg II time-lag difference between the blue and red wings is larger than that of C IV, which leads to larger line-shift variability of Mg II.

For C IV, high-blueshift sources tend to have small line-shift variability. This connection might simply reflect the fact that, as mentioned in Section 5.2, high-blueshift sources are less variable in terms of quasar continua. However, the evolution of VAR.($V_{\rm shift,Mg\ II,\ se}$) along the C IV blueshift is not entirely expected. The evolution can only be explained if the time-lag difference of the blue and red wings and/or the ratio of the radial motions to the virial motions increases with Eddington ratio. Such a correlation may exist because the ratio of the radiative force to the gravitational potential of the SMBH increases with the Eddington ratio (e.g., Shakura & Sunyaev 1973). The radiative pressure can help generate non-virial motions in the BLR.

5.5. Is Eddington Ratio the Sole Factor?

As we discussed above, our results can be explained if the C IV blueshift is driven by the Eddington ratio (which is the driver of the quasar main sequence; see, e.g., Boroson & Green 1992; Sulentic et al. 2000b; Shen & Ho 2014). However, is the Eddington ratio the sole factor to determine the C IV blueshift? Figure 25 presents the Eddington ratio as a function of the C IV blueshift. In general, the Eddington ratio and the C IV blueshift tend to be anti-correlated. However, some extreme blueshift sources have low Eddington ratios, similar to those of no blueshift sources. This could simply be caused by the $M_{\rm BH}$ estimation bias discussed above. However, there are high Eddington-ratio sources that show almost no blueshift. There are several possibilities for these sources. For instance, the high Eddington ratio might be a necessary but insufficient condition for driving accretion-disk winds (Baskin & Laor 2005; Coatman et al. 2016). Another possibility is that the $M_{\rm BH}$ estimator we adopted in this work (i.e., the Mg II single-epoch virial $M_{\rm BH}$ estimator; see Section 2.2) has significant intrinsic scatter ($\geqslant$0.4 dex; see, e.g., Vestergaard & Peterson 2006) and suffers from considerable Eddington biases (Shen & Kelly 2010). These speculations can be tested by controlling the Eddington ratio and exploring the blueshift as a function of quasar luminosity or other properties. Unfortunately, such a study requires an unbiased estimation of $M_{\rm BH}$ over the entire quasar population, which is presently unavailable. The ongoing RM campaigns, such as SDSS-RM (Shen et al. 2015) and other multi-object RM campaigns (King et al. 2015), have the potential to effectively test our scenario.

6. Summary and Conclusion

We have investigated the C IV blueshift as a function of quasar properties, and constrained the intrinsic variability of the C IV blueshift in single-epoch spectra using the 29 epochs of SDSS-RM spectra. Our primary results are as follows.

1. We confirmed that the extreme blueshift sources generally have small EWs, while the reverse is not true (Figure 4) with our high S/N composite spectra. Other high-ionization emssion lines, such as He II, also show a blueshift, and the blueshift velocities are correlated with those of C IV (Figure 6). Furthermore, the dependence of the He II blueshift on EWs is similar to that of C IV (Figure 7). These results suggest that the blueshift behavior is common for high-ionization emission lines (Section 3.1).
2. Compared with Mg II, C IV is preferentially suppressed for the extreme blueshift sources (Figure 8). This result indicates a reduction of the high-energy ionizing continuum over the low-energy one (Section 3.1).
3. FWHM$_{\rm C\ IV}$/FWHM$_{\rm Mg\ II}$ anti-correlates with the C IV blueshift (Figure 9). Similar relations are also found for $\sigma_{\rm C\ IV}/\sigma_{\rm Mg\ II}$, albeit the correlation is not apparent at the extreme blueshift (Figure 10). These relations can be used to make corrections for the C IV $M_{\rm BH}$ estimators (Section 3.2).
4. We also investigated the line-shift variability of Mg II (Figure 12) and C IV (Figure 13). The line-shift variability of C IV and Mg II are different in terms of variability amplitude and their relation with the C IV blueshift. These differences indicate that the structures of C IV and Mg II evolve differently as a function of the C IV blueshift (Sections 4.1 and 4.2). We also found that quasar variability can slightly enhance the connection between the C IV blueshift and EW (Figure 22; Section 5.1)
5. We presented the variability of quasar continua as a function of the C IV blueshift. The extreme blueshift sources are less variable (Figure 24), indicating that the high-blueshift sources tend to have high Eddington ratios (Figure 23, Section 5.2).
6. All of these results can be explained if quasar SEDs become softer with increasing Eddington ratios and with the presence of X-ray shielding by the inner accretion disk. However, a high Eddington ratio might be an insufficient condition for the C IV blueshift (Figure 25). Future multi-object RM experiments can probe our scenario.

M.Y.S. thanks K. D. Denney for a beneficial discussion. We thank the anonymous referee for helpful comments that improved the paper. M.Y.S. and Y.Q.X. acknowledge the support from NSFC-11603022, NSFC-11473026, NSFC-11421303, the 973 Program (2015CB857004), the China Postdoctoral Science Foundation (2016M600485), the CAS Frontier Science Key Research Program (QYZDJ-SSW-SLH006), and the Fundamental Research Funds for the Central Universities. W.N.B. acknowledges support from NSF Grant AST-1516784 and *Chandra* X-ray Center grant GO6-17083X.

Funding for SDSS-III has been provided by the Alfred P. Sloan Foundation, the Participating Institutions, the National Science Foundation, and the U.S. Department of Energy Office of Science. The SDSS-III web site is http://www.sdss3.org/.

SDSS-III is managed by the Astrophysical Research Consortium for the Participating Institutions of the SDSS-III Collaboration including the University of Arizona, the Brazilian Participation Group, Brookhaven National Laboratory, Carnegie Mellon University, University of Florida, the French Participation Group, the German Participation Group, Harvard University, the Instituto de Astrofisica de Canarias, the Michigan State/Notre Dame/JINA Participation Group, Johns Hopkins University, Lawrence Berkeley National Laboratory, Max Planck Institute for Astrophysics, Max Planck Institute for Extraterrestrial Physics, New Mexico State University, New York University, Ohio State University, Pennsylvania State University, University of Portsmouth, Princeton University, the Spanish Participation Group, University of Tokyo, University of Utah, Vanderbilt University, University of Virginia, University of Washington, and Yale University.

Software: Astropy (Astropy Collaboration et al. 2013), Kapteyn (Terlouw & Vogelaar 2015), Matplotlib (Hunter 2007), Numpy & Scipy (Van Der Walt et al. 2011).

ORCID iDs

Mouyuan Sun https://orcid.org/0000-0002-0771-2153
Yongquan Xue https://orcid.org/0000-0002-1935-8104
Gordon T. Richards https://orcid.org/0000-0002-1061-1804
Jonathan R. Trump https://orcid.org/0000-0002-1410-0470
Yue Shen https://orcid.org/0000-0003-1659-7035
W. N. Brandt https://orcid.org/0000-0002-0167-2453

References

Abramowicz, M. A., Czerny, B., Lasota, J. P., & Szuszkiewicz, E. 1988, ApJ, 332, 646
Ai, Y. L., Yuan, W., Zhou, H. Y., et al. 2010, ApJL, 716, L31
Astropy Collaboration, Robitaille, T. P., Tollerud, E. J., et al. 2013, A&A, 558, A33
Bachev, R., Marziani, P., Sulentic, J. W., et al. 2004, ApJ, 617, 171
Baldwin, J. A. 1977, ApJ, 214, 679
Barth, A. J., Bennert, V. N., Canalizo, G., et al. 2015, ApJS, 217, 26
Baskin, A., & Laor, A. 2004, MNRAS, 350, L31
Baskin, A., & Laor, A. 2005, MNRAS, 356, 1029
Bolton, A. S., Schlegel, D. J., Aubourg, É., et al. 2012, AJ, 144, 144
Boroson, T. A., & Green, R. F. 1992, ApJS, 80, 109
Brotherton, M. S., Runnoe, J. C., Shang, Z., & DiPompeo, M. A. 2015, MNRAS, 451, 1290
Chajet, L. S., & Hall, P. B. 2013, MNRAS, 429, 3214
Chajet, L. S., & Hall, P. B. 2017, MNRAS, 465, 1741
Coatman, L., Hewett, P. C., Banerji, M., et al. 2017, MNRAS, 465, 2120
Coatman, L., Hewett, P. C., Banerji, M., & Richards, G. T. 2016, MNRAS, 461, 647
Corbin, M. R. 1990, ApJ, 357, 346
Dawson, K. S., Schlegel, D. J., Ahn, C. P., et al. 2013, AJ, 145, 10
Denney, K. D. 2012, ApJ, 759, 44
Denney, K. D., Horne, K., Brandt, W. N., et al. 2016, ApJ, 833, 33
Denney, K. D., Horne, K., Shen, Y., et al. 2016, ApJS, 224, 14
Denney, K. D., Peterson, B. M., Pogge, R. W., et al. 2009, ApJL, 704, L80
Dietrich, M., Hamann, F., Shields, J. C., et al. 2002, ApJ, 581, 912
Dong, X.-B., Wang, T.-G., Wang, J.-G., et al. 2009, ApJL, 703, L1
Du, P., Lu, K.-X., Zhang, Z.-X., et al. 2016, ApJ, 825, 126
Eisenstein, D. J., Weinberg, D. H., Agol, E., et al. 2011, AJ, 142, 72
Fine, S., Croom, S. M., Bland-Hawthorn, J., et al. 2010, MNRAS, 409, 591
Gaskell, C. M. 1982, ApJ, 263, 79
Gaskell, C. M. 2009, NewAR, 53, 140
Giveon, U., Maoz, D., Kaspi, S., Netzer, H., & Smith, P. S. 1999, MNRAS, 306, 637
Grier, C. J., Peterson, B. M., Horne, K., et al. 2013, ApJ, 764, 47
Gunn, J. E., Siegmund, W. A., Mannery, E. J., et al. 2006, AJ, 131, 2332
Guo, H., & Gu, M. 2016, ApJ, 822, 26
Hou, A., Parker, L. C., Harris, W. E., & Wilman, D. J. 2009, ApJ, 702, 1199
Hunter, J. D. 2007, CSE, 9, 90
Jiang, Y.-F., Stone, J. M., & Davis, S. W. 2014a, ApJ, 784, 169
Jiang, Y.-F., Stone, J. M., & Davis, S. W. 2014b, ApJ, 796, 106
Kelly, B. C. 2007, ApJ, 665, 1489
Kelly, B. C., Treu, T., Malkan, M., Pancoast, A., & Woo, J.-H. 2013, ApJ, 779, 187
Kilerci Eser, E., Vestergaard, M., Peterson, B. M., Denney, K. D., & Bentz, M. C. 2015, ApJ, 801, 8
King, A. L., Martini, P., Davis, T. M., et al. 2015, MNRAS, 453, 1701
Korista, K. T., & Goad, M. R. 2004, ApJ, 606, 749
Kozłowski, S. 2016, ApJ, 826, 118
Krawczyk, C. M., Richards, G. T., Mehta, S. S., et al. 2013, ApJS, 206, 4
Leighly, K. M. 2004, ApJ, 611, 125
Leighly, K. M., Halpern, J. P., Jenkins, E. B., & Casebeer, D. 2007, ApJS, 173, 1
Luo, B., Brandt, W. N., Alexander, D. M., et al. 2014, ApJ, 794, 70
Luo, B., Brandt, W. N., Hall, P. B., et al. 2015, ApJ, 805, 122
Lusso, E., Comastri, A., Simmons, B. D., et al. 2012, MNRAS, 425, 623
MacLeod, C. L., Ivezić, Ž., Kochanek, C. S., et al. 2010, ApJ, 721, 1014
Marziani, P., Martínez Carballo, M. A., Sulentic, J. W., et al. 2016, Ap&SS, 361, 29
Marziani, P., Sulentic, J. W., Dultzin-Hacyan, D., Calvani, M., & Moles, M. 1996, ApJS, 104, 37
Marziani, P., Sulentic, J. W., Negrete, C. A., et al. 2010, MNRAS, 409, 1033
Marziani, P., Sulentic, J. W., Plauchu-Frayn, I., & del Olmo, A. 2013, ApJ, 764, 150
Murray, N., & Chiang, J. 1997, ApJ, 474, 91
Plotkin, R. M., Shemmer, O., Trakhtenbrot, B., et al. 2015, ApJ, 805, 123
Proga, D., Stone, J. M., & Kallman, T. R. 2000, ApJ, 543, 686
Richards, G. T., Kruczek, N. E., Gallagher, S. C., et al. 2011, AJ, 141, 167
Richards, G. T., Lacy, M., Storrie-Lombardi, L. J., et al. 2006, ApJS, 166, 470
Richards, G. T., Vanden Berk, D. E., Reichard, T. A., et al. 2002, AJ, 124, 1
Rumbaugh, N., Shen, Y., Morganson, E., et al. 2017, arXiv:1706.07875
Runnoe, J. C., Brotherton, M. S., DiPompeo, M. A., & Shang, Z. 2014, MNRAS, 438, 3263
Runnoe, J. C., Brotherton, M. S., Shang, Z., & DiPompeo, M. A. 2013, MNRAS, 434, 848
Sądowski, A., Narayan, R., McKinney, J. C, & Tchekhovskoy, A. 2014, MNRAS, 439, 503
Shakura, N. I., & Sunyaev, R. A. 1973, A&A, 24, 337
Shemmer, O., & Lieber, S. 2015, ApJ, 805, 124
Shen, Y. 2013a, BASI, 41, 61
Shen, Y., Brandt, W. N., Dawson, K. S., et al. 2015, ApJS, 216, 4
Shen, Y., Brandt, W. N., Richards, G. T., et al. 2016, ApJ, 831, 7
Shen, Y., Greene, J. E., Strauss, M. A., Richards, G. T., & Schneider, D. P. 2008, ApJ, 680, 169
Shen, Y., & Ho, L. C. 2014, Natur, 513, 210
Shen, Y., & Kelly, B. C. 2010, ApJ, 713, 41
Shen, Y., & Liu, X. 2012, ApJ, 753, 125
Shen, Y., Liu, X., Loeb, A., & Tremaine, S. 2013b, ApJ, 775, 49
Shen, Y., Richards, G. T., Strauss, M. A., et al. 2011, ApJS, 194, 45
Smee, S. A., Gunn, J. E., Uomoto, A., et al. 2013, AJ, 146, 32

Sulentic, J. W., Bachev, R., Marziani, P., Negrete, C. A., & Dultzin, D. 2007, ApJ, 666, 757
Sulentic, J. W., del Olmo, A., Marziani, P., et al. 2017, A&A, 608, A122
Sulentic, J. W., Marziani, P., & Dultzin-Hacyan, D. 2000a, ARA&A, 38, 521
Sulentic, J. W., Zwitter, T., Marziani, P., & Dultzin-Hacyan, D. 2000b, ApJL, 536, L5
Sun, M., Trump, J. R., Shen, Y., et al. 2015, ApJ, 811, 42
Sun, Y.-H., Wang, J.-X., Chen, X.-Y., & Zheng, Z.-Y. 2014, ApJ, 792, 54
Terlouw, J. P., & Vogelaar, M. G. R. 2015, Kapteyn Package, version 2.3, Groningen, http://www.astro.rug.nl/software/kapteyn/
Trakhtenbrot, B., & Netzer, H. 2012, MNRAS, 427, 3081
Trump, J. R., Impey, C. D., Kelly, B. C., et al. 2009, ApJ, 700, 49
Van Der Walt, S., Colbert, S. C., & Varoquaux, G. 2011, MCSE, 13, 22
Vanden Berk, D. E., Wilhite, B. C., Kron, R. G., et al. 2004, ApJ, 601, 692
Vasudevan, R. V., & Fabian, A. C. 2007, MNRAS, 381, 1235
Vestergaard, M., & Osmer, P. S. 2009, ApJ, 699, 800
Vestergaard, M., & Peterson, B. M. 2006, ApJ, 641, 689
Vestergaard, M., & Wilkes, B. J. 2001, ApJS, 134, 1
Wang, H., Wang, T., Zhou, H., et al. 2011, ApJ, 738, 85
Wang, J.-M., & Netzer, H. 2003, A&A, 398, 927
Wilhite, B. C., Vanden Berk, D. E., Brunner, R. J., & Brinkmann, J. V. 2006, ApJ, 641, 78
Wilkes, B. J. 1986, MNRAS, 218, 331
Wu, J., Brandt, W. N., Hall, P. B., et al. 2011, ApJ, 736, 28
Wu, J., Vanden Berk, D. E., Brandt, W. N., et al. 2009, ApJ, 702, 767
Zhu, F.-F., Wang, J.-X., Cai, Z.-Y., & Sun, Y.-H. 2016, ApJ, 832, 75